

Highly coherent frequency-entangled photons based on parametric instability in active fiber ring cavity

Lei Gao (✉ gaolei@cqu.edu.cn)

Chongqing University

Ziwei Li

Chongqing University

Hongqing Ran

Chongqing University

Yulong Cao

Chongqing University

Stefan Wabnitz

Chongqing University

Zinan Xiao

Shiyun Dai

Qiang Wu

Lingdi Kong

Ligang Huang

Wei Huang

Tao Zhu

Article

Keywords:

Posted Date: December 16th, 2021

DOI: <https://doi.org/10.21203/rs.3.rs-1138069/v1>

License:  This work is licensed under a Creative Commons Attribution 4.0 International License.

[Read Full License](#)

Highly coherent frequency-entangled photons based on parametric instability in active fiber ring cavity

LEI GAO^{1,*}, ZIWEI LI¹, HONGQING RAN¹, YULONG CAO¹, STEFAN WABNITZ^{2,3}, ZINAN XIAO¹, SHIYUN DAI¹, QIANG WU¹, LINGDI KONG¹, LIGANG HUANG¹, WEI HUANG¹, AND TAO ZHU¹

Highly coherent frequency-entangled photons at telecom band are critical in quantum information protocols and quantum tele-communication. Photon pairs generated by spontaneous parametric down-conversion in nonlinear crystals or modulation instability in optical fibers exhibit random fluctuations. Here, we demonstrate highly stable frequency-entangled photons based on parametric instability in an active fiber ring cavity, where periodic modulation of dispersion excites parametric resonance, and the characteristic wave number is selected by the periodic modulation of resonator. Background-free autocorrelation of single-shot spectra reveals that spectra of parametric instability sidebands possess high coherence. The quantum properties are tested by the Hanbury Brown-Twiss measurement and Hong-Ou-Mandel interference. We conform the frequency-entanglement of two parametric instability sidebands by a spatial quantum beating with a fringe visibility of 97.9%. Our results prove that the parametric instability in active fiber cavity is effective to generate highly coherent frequency-entangled photon pairs, which would facilitate subsequent quantum applications.

¹Key Laboratory of Optoelectronic Technology & Systems (Ministry of Education), Chongqing University, Chongqing 400044, China

²Dipartimento di Ingegneria dell'Informazione, Elettronica e Telecomunicazioni, Sapienza Università di Roma, via Eudossiana 18, 00184 Roma, Italy.

³Novosibirsk State University, 1 Pirogova str, Novosibirsk 630090, Russia.

*email: gaolei@cqu.edu.cn

As non-classical optical sources, quantum-entangled photons are critical for testifying fundamental quantum mechanisms, such as quantum cryptography [1,2], quantum communications [3], quantum computing [4], violation of Bell inequalities [5]. Specially, frequency-entangled photons have been utilized to cancel dispersion in interferometers, and to improve clock synchronization [6,7]. Spontaneous parametric down conversion in nonlinear bulk crystal and waveguide with high χ^2 nonlinearity is frequently utilized for entangled photon pairs with high brightness [8–10]. However, challenges remain due to relative high material dispersion, where phase-matching conditions are deteriorated for long interacting length, reducing conversion efficiency. Other drawbacks include multi-mode characteristics, which require precise fiber-coupling alignment for quantum telecommunication.

Spontaneous four-wave-mixing process based on χ^3 nonlinearity is identified to be a promising candidate for producing reliable entangled photon pairs [11–15]. The modulation instability (MI) in optical fibers has been widely used to generate photon pairs with controllable frequency and polarization. When the phase-matching conditions are satisfied, signal and idler photons are produced simultaneously at the expense of annihilation of two identical pump photons. Numerous schemes have been carried out based on single-mode fiber [16], birefringence fiber [17], and photonic crystal fiber [18]. However, recent single-shot detections shown that the spectra produced by spontaneous MI process exhibits great fluctuations for consecutive roundtrips [19]. Thus, the corresponding photon pairs within different roundtrips are different. For example, the photon numbers and phases may vary for different roundtrips. As the coherence of the MI spectra is relatively low, the correlation time of the photon pairs is small, making it difficult for multiphoton nonlocality and quantum teleportation [20]. In many experiments, optical filters with narrow bandwidth are utilized to increasing the coherence time [21]. Yet, as a post-selection, optical filtering does not suppress the fluctuations of the MI spectra.

Recently, we found that the parametric instability (PI) produces gain sidebands with high coherence [22,23], which facilitates generation of indistinguishable photon pairs, for example, with constant photon numbers and phases. As shown in Fig. 1(a), the PI is induced by parametric resonance due to periodic modulation of dispersion. Different from the MI, where symmetry breaking bifurcation favors the growth of modulation gains, the characteristic wave number in the PI is selected by the periodic modulation of resonator dispersion [22–27]. It is also known as the Faraday instability. This unique instability has been identified in fluids [28], Bose condensates [29], and nonlinear optics [30], where stable patterns are observed. When PI is excited in cavity, resonating can reduce the bandwidth of sidebands to a much narrower level [31–33]. The most intriguing property of PI in cavity-enhanced schemes are the fixed phases among consecutive photon pairs. Namely, the

initial phase of each photon, ϕ_0 , is determined by the resonating condition,

$$\phi_0 + knL = 2\pi m \quad (1)$$

where, k is the wave vector, $m=1,2,\dots$, n is the refractive index, L is the cavity length. The identical initial phase makes the photon pairs indistinguishable for consecutive roundtrips. This consistency highly facilitates the subsequent applications, such as quantum computation and quantum processing.

In this article, we demonstrate the generation of highly coherent frequency-entangled photons with narrow bandwidth based on PI in an active fiber ring cavity. The cavity consists two sections of fibers. One fiber possesses normal dispersion, while the other is anomalous dispersed. Specifically, a section of erbium doped fiber is optically pumped as the gain. When the PI arises, fundamental Stokes and anti-Stokes sidebands are excited. By performing the dispersive Fourier transformation detection (DFT), the corresponding single-shot spectra reveal that the PI sidebands are identical. The Hanbury Brown-Twiss (HBT) measurement proves that the generated photon pairs exhibit high coherence time. Besides, we demonstrate the frequency-entanglement by spatial quantum beating in Hong-Ou-Mandel (HOM) interference detection based on a fiber-based Mach-Zehnder interferometer (MZI) without any stabilization feedback.

Results and discussion

Experimental realization of frequency-entangled photons. The experimental system is schematically depicted in Fig.1(c), where PI is excited in an active ring fiber cavity with net normal dispersion of 0.863 ps^2 . (See “Methods” section for details) The highly coherent PI spectra within consecutive round trips make it possible for excitation of frequency-entangled photon pairs with high consistency. To testify their non-classical behavior, we perform both the HOM interference and HBT detections. Figure 1(b) exhibits the HOM interference scheme, where the relative time delay of two paths is adjusted by a delay line (DL). After optical coupler 4 (OC4, 50:50), photons in two paths are filtered by two filters, then, coincidence counting (CC) is registered after simultaneous photon detections by two single photon detectors (SPDs). The photons for the input ports of OC4 can be either ω_1 or ω_2 . Therefore, there are eight possible routines. When photon pair is indistinguishable, the coincidence probability of photon pair after interferometer is determined by the biphoton spectral amplitude, the relative delay time, and the bandwidth of photon field [34–39]. Based on a multimode theory [37], for a filter with Gaussian spectrum, the normalized coincidence counts for above two-photon interference configuration can be expressed as

$$P \propto 1 - V \operatorname{sinc}(\sigma\tau) \cos[(\omega_1 - \omega_2)\tau] \quad (2)$$

where, V is the visibility, and τ represents the optical time delay between the two paths. σ is the angular frequency bandwidth of the filters. (See “Methods” section for details of measurement)

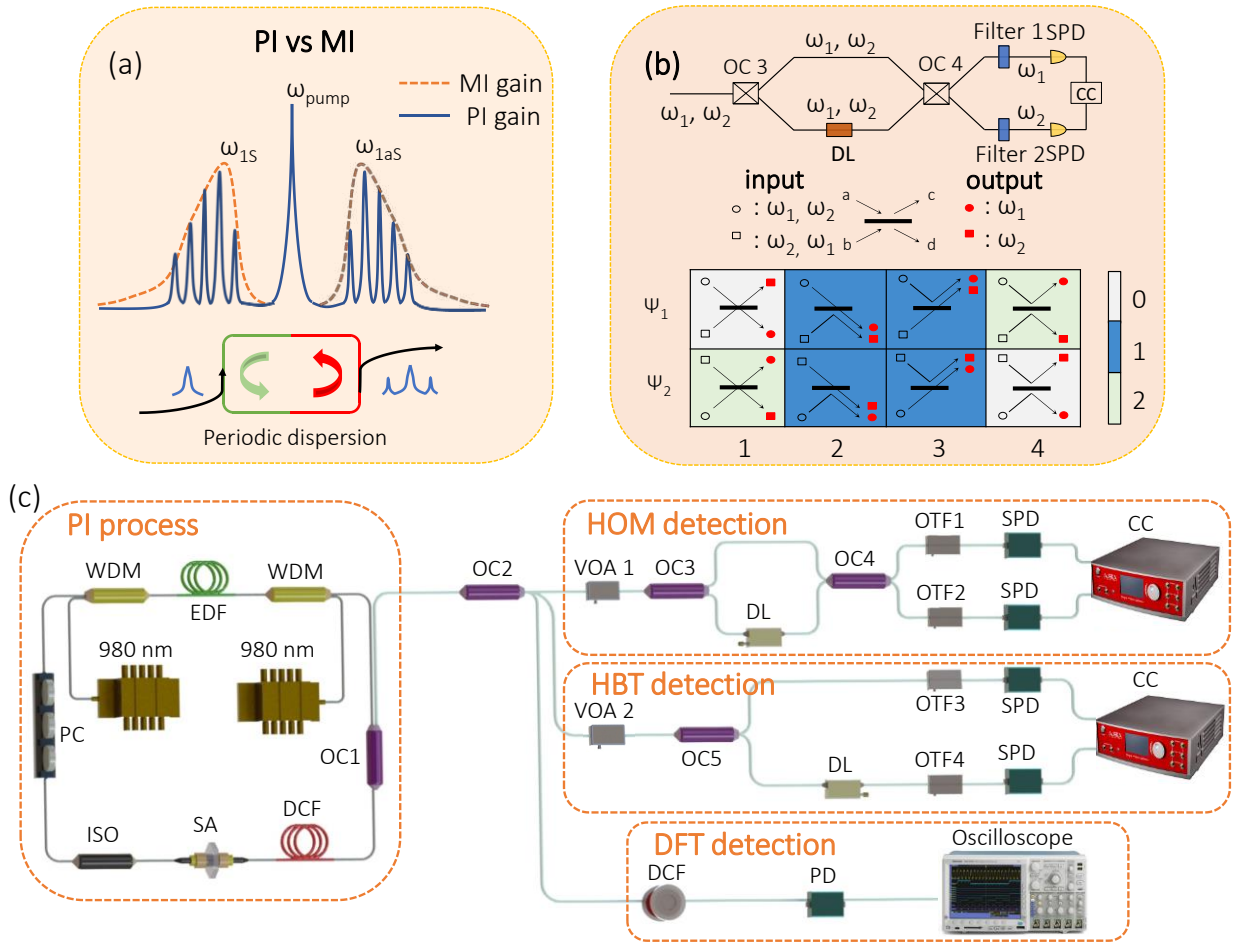


FIG. 1. Main experimental apparatus. (a) Scheme of PI in resonator with periodic dispersion vs MI. (b) Scheme of HOM interference. The different colors represent the number of detected photons. (c) Experimental setup for the frequency-entangled photon pairs based on PI in active fiber ring cavity, and the detail measurements.

By rotating polarization controller properly, PI can be excited with easiness. The temporal pulse train is shown in Fig. 2(b), where a period of 146 ns matches well with the cavity length. The averaged optical spectrum in Fig. 2(c) possesses a center wavelength λ_0 at 1561.19 nm operating in quasi-continuous wave (quasi-CW) mode, and two sidebands, namely, $\lambda_{\text{as}}=1558.048$ nm, $\lambda_{\text{s}}=1564.338$ nm. The fundamental sideband spacing is 393 GHz, which is in accordance with the calculated value in Fig. 2(a) for an estimated intracavity peak power of 25.8 W. We have checked experimentally that the states of polarization of the two sidebands are identical. The normalized single-shot spectra within 50 consecutive roundtrips shown in Fig. 3(a) clearly exhibit high consistency. The strong CW component is filtered automatically by the DFT. We observe well-fixed fine structures in the real-time optical spectra for the two sidebands, which are invisible in the averaged optical spectrum (Fig. 2(c)). These highly identical PI spectra are totally different from the randomly evolving sidebands in MI in conventional SMF [19]. A frequency width of ~ 12 GHz is shown for the subpeaks in both Stokes and anti-Stokes sidebands. It is interesting to remember that the resolution of the DFT detection is only 0.2 nm. Therefore, the observed width of subpeaks maybe not accurate enough, yet, they denote that the subpeaks formed due to PI within active fiber cavity possess narrow width, thus, high coherence.

The parametric resonance in cavity configuration make it possible to tune the frequency shift of the PI sidebands via

dispersion management. We vary the net dispersion via adjusting the optical length of single mode fiber (SMF), and Fig. 2(d) depicts the obtained sideband shift as a function of net dispersion. The solid dots together with linear fitting denote the tuning flexibility of nondegenerate PI sidebands by dispersion management, which highly facilitates the generation of tunable photon pairs.

High consistency of PI sidebands. The high consistency of the PI sidebands can be verified quantitatively by the background-free correlations of the fundamental anti-Stokes and Stokes sidebands as

$$\zeta = \langle S_n * S_n \rangle - \langle S_n \rangle * \langle S_n \rangle \quad (3)$$

which presents the average spectral autocorrelation of all single-shot spectra S_n by subtracting the autocorrelation of the averaged spectrum [19]. The coherence statistics of the two sidebands are depicted in Figs. 3(b) and 3(c). The positive central peak at zero frequency shift arises from the narrow lines in the single-shot spectra, whereas fluctuations at larger frequency shift denote cooperative (positive value) and competitive (negative value) interactions of the individual cavity modes [41]. Both autocorrelation analysis for the Stokes and anti-Stokes regions show quasi-periodicity along the frequency shift, indicating strong correlation among the single-shot spectra.

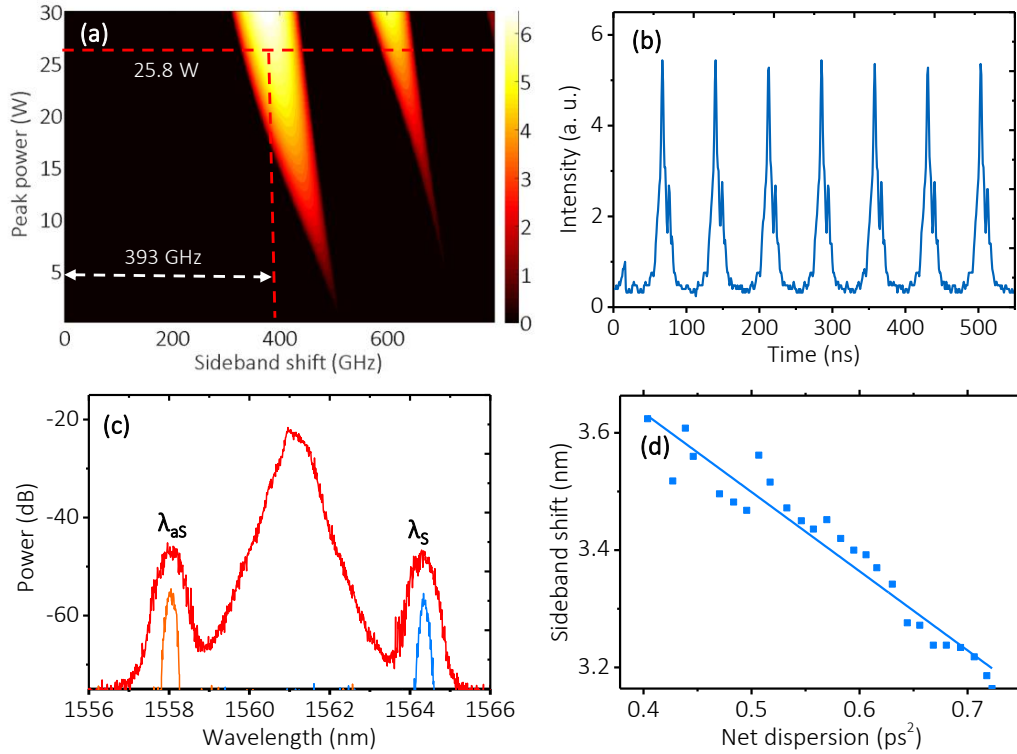


FIG.2. Characteristics of PI sidebands. (a) Simulation results of PI sidebands. The dotted sideband shift for the peak power of 25.8 W is about 393 GHz. (b) Temporal train of pulses. (c) Optical spectrum of pulses, and two filtered wavelengths of two channels. (d) Sideband shift vs net dispersion of the PI cavity. The experimental data is fitted linearly.

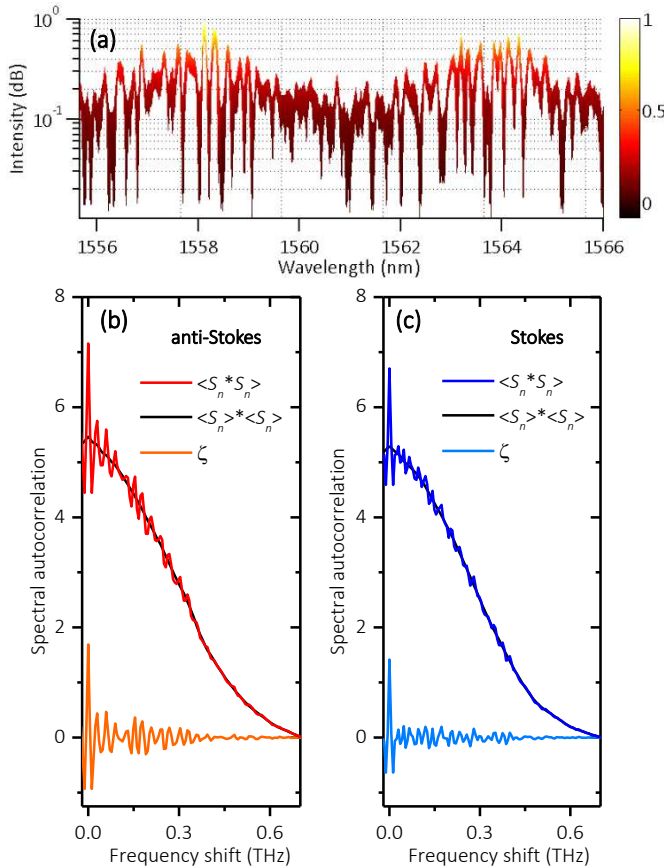


FIG. 3. Real time characteristics of PI sidebands. (a) 50 consecutive single-shot spectra of the Stokes and anti-Stokes sidebands with normalized intensities. (b)-(c) Back-ground free

autocorrelation of anti-Stokes (from 1555.6 nm to 1561.2 nm) and Stokes (from 1561.2 nm to 1566.8 nm) computed from the single-shot spectra in (a).

The PI sidebands with high coherence make it possible to generate frequency-entangled photons with high quality. To test the quantum performance, we filter the signal and idler channels, respectively. Here, the average power for each filtered channel is -49.6 dBm, which is close to the detection limit of SPDs (-45 dBm). The corresponding photon count rate for each channel is 80 kcps. Considering the trigger rate of 1.25 MHz, and the quantum efficiency of 20%, the corresponding average photon number is about 0.32 per pulse. This photon statistic is far away from the standard Poisson distribution for single photons with a mode number of 1 [42]. As the repetition rate of 6.84 MHz, the production rate is high, which is impossible to be characterized by photon counting technique. Therefore, the pulse intensity has to be attenuated. Different photon count rates can be recorded for various attenuations. For the attenuated pulses, a reliable average photon number less than 0.01 is required for approximately Poisson distribution [42,43]. Here, the counting rate is set as 2 kcps, and the average photon number is 0.008.

Spectral correlation properties. The spectral correlation of the photon pair is revealed by the joint spectral intensity (JSI). We filter the Stokes wavelength via optical tunable filter 3 (OTF3), while the anti-Stokes wavelength via OTF4, and scan the center wavelengths around the two sidebands with a step of 0.05 nm, respectively. Fig. 4 show the obtained JSI function distribution, which is fitted by a two-dimensional Gaussian function. Clear positive frequency correlation is seen for the two channels.

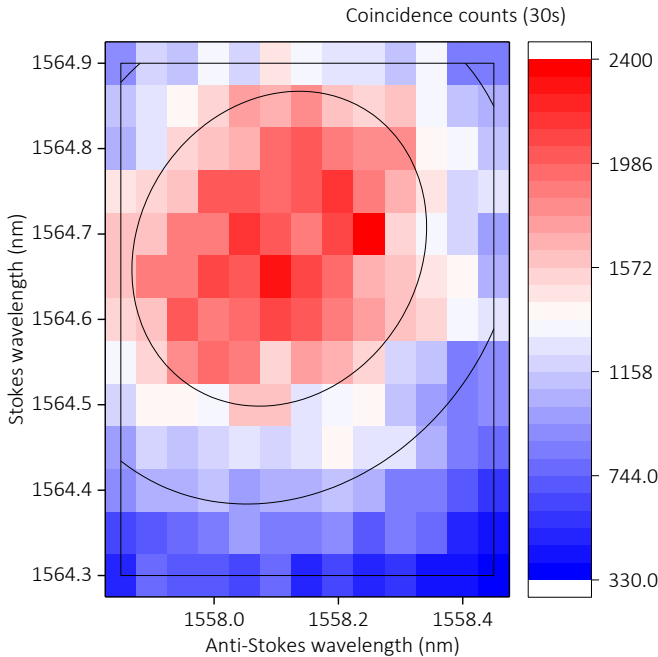


Fig. 4 Measured JSI distribution for the two sidebands of PI. The obtained coincidence counts are fitted by a Gaussian function.

Temporal correlation properties. To identify the temporal correlation of the photon pair, we perform a HBT detection, where the detected signal of one SPD triggers the other with a temporal step of 1 ns. Figures 5(a)-(b) denote two typical histograms of CCs as a function of time delay between the two channels within 30 s, which are fitted with an exponential shape [31]. The CCs induced by dark counts were measured to be less

than 5 cps, therefore, their contribution was negligible, and they were not subtracted from the raw data. It is clear that for all the two cases, the CCs and the fitting curves fits well. The correlation times for two channels of Stokes ($\lambda_S-\lambda_S$) and anti-Stokes ($\lambda_{AS}-\lambda_{AS}$) are 3.66 ns, and 3.20 ns, respectively. This proves that the formed photon pairs have similar correlation properties for the two channels. Slightly asymmetry is also shown for the two sidebands. Besides, the produced photon pairs are rather stable. The quantum correlation among photon pairs in consecutive roundtrips is further tested by inserting SMFs with different lengths. Figure 5(c) depict the CCs within 19 consecutive photon pairs for the Stokes channels. They fluctuate within a range of 14.96%, which are mainly induced by the intrinsic probabilistic characteristics of the spontaneous PI and optical attenuation process.

In the HBT measurement, the large correlation time (or small effective bandwidth) is not determined by the optical filters (0.2 nm), but the bandwidth of the subpeaks. Considering the correlation time of 3.66 ns/3.20 ns, the effective bandwidth of subpeaks may be less than 0.06 GHz [31]. This denotes that the frequency width of the subpeaks within the single-shot spectra is not as large as ~12 GHz for both Stokes and anti-Stokes sidebands. Namely, the obtained DFT data is not accurate enough, which needs further more precise investigation. Yet, the large correlation time of the HBT measurement do prove that the stability of photon numbers within consecutive roundtrips is improved, which is totally different from the fluctuating numbers and extremely large bandwidth for photons based on spontaneous parametric down-conversion in nonlinear crystals or MI in optical fibers.

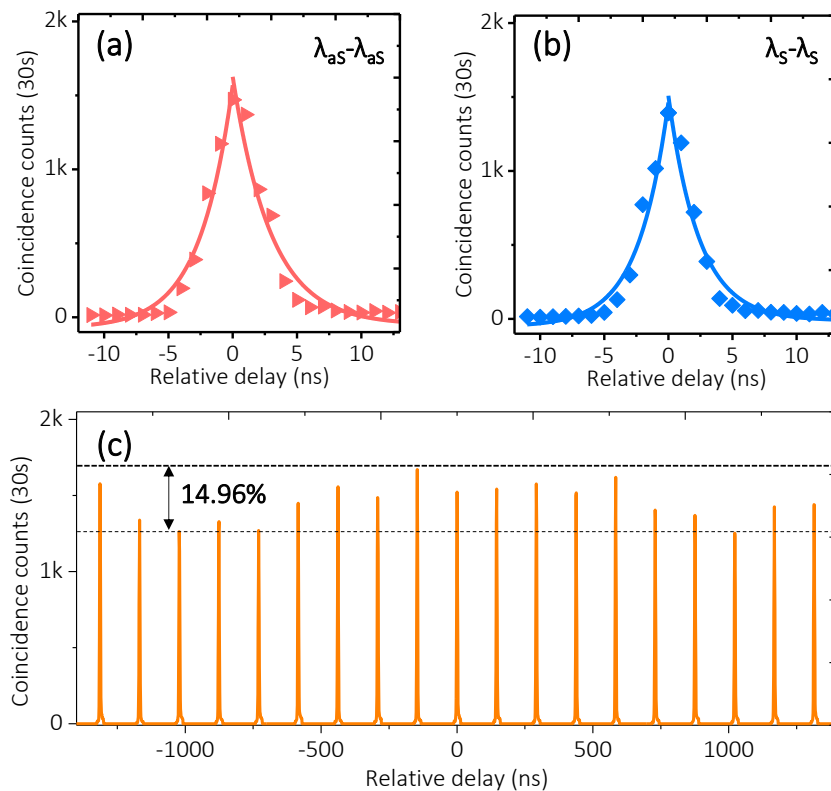


FIG. 5. HBT measurement results. (a)-(b) Coincidence counts for two channels of anti-Stokes ($\lambda_{AS}-\lambda_{AS}$) sideband and Stokes ($\lambda_S-\lambda_S$) sideband, respectively. The photon count rate is 2 kcps. They are fitted exponentially. (c) Coincidence counts of photon pairs within 19 roundtrips for Stokes sideband.

Two photon interference results. The frequency-entanglement can be confirmed by the HOM interference measurement. The center wavelength of two nondegenerate sidebands are filtered by the two OTFs, respectively. The coincidence counts are measured as a function of optical path via detuning DL. Before entering the OC4, the states of polarization of the two wavelengths are copolarized to ensure indistinguishability. On one side, the HOM interference measurement is performed when the OTFs are adjusted for the same wavelength, namely, the Stokes or anti-Stokes wavelengths. Conventional HOM dip patterns are observed for the two cases, as depicted in Fig. 6 (a) for the anti-Stokes sideband, where each data is detected within 30 s. We also neglect the contribution from dark counts. For both cases, when the path difference approach to zero, two photon interference occurs. The destructive HOM interference results into a minimum coincidence count. The experimental trace is fitted by the formula 2. Here, the raw visibility for anti-Stokes sideband is 76.3%. The corresponding net visibility by subtracting the accidental coincidence is 84.3%. The corresponding full width at half maximum width is ~9.14 mm, which is mainly determined by the filter bandwidth of 0.2 nm. This large bandwidth makes more than one subpeaks account for the coincidence detection. The HOM visibility can be further improved by optimizing the splitting ratio of OC, the polarization dependence of the optical devices, and most importantly, the path difference fluctuations due to temperature variations and wind vibrations in the laboratory [41].

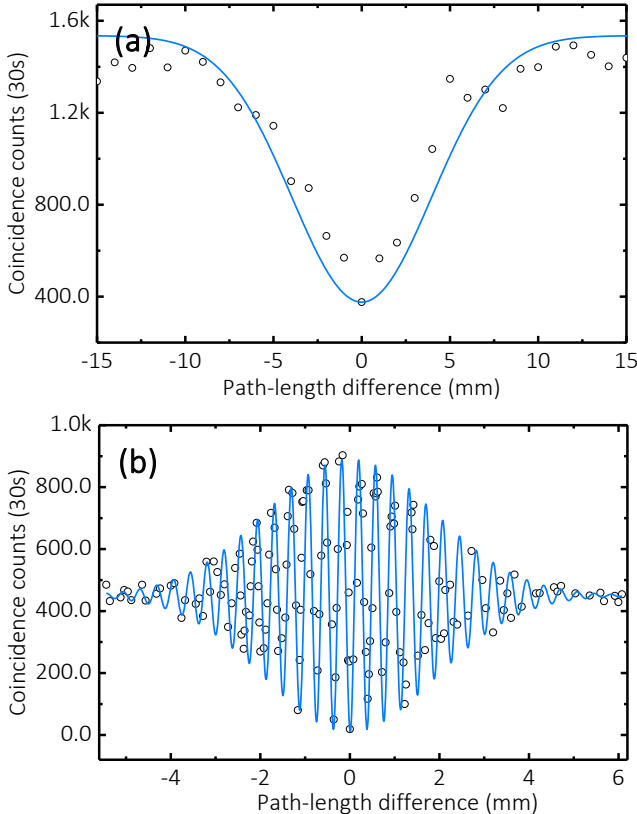


FIG. 6. HOM measurement results. (a) Conventional dip type for anti-Stokes sideband. The coincidence counts as a function of path-difference, superimposed by a Gaussian fitting curve. (b) Coincidence counts as a function of path-difference between anti-Stokes and Stokes sidebands. The spatial quantum beating demonstrates the frequency-entanglement.

On the other side, spatial quantum beating is observed when the wavelengths of the two OTFs are adjusted to be the centers of Stokes and anti-Stokes sidebands, respectively. Fig. 6 (b) shows the experimental coincidence counts after subtracting accidental coincidence counts. After fitting, the visibility is 97.9%. The modulation period of the spatial quantum beating fringe is 3.75 mm, which is coincidence to the theoretically estimated value of 3.8 mm. The high consistency of experiments with theoretical predication of nonclassical two photon interference demonstrates that highly coherent frequency-entangled two photon state can be prepared via PI in active fiber ring cavity.

Conclusion

We have developed and characterized a highly coherent fiber-based frequency-entangled photon pairs. Periodic dispersion management in active fiber ring cavity excites PI, where Stokes and anti-Stokes sidebands are formed due to degenerate four-wave-mixing. The single-shot spectra reveal that the sidebands possess subpeaks with narrow bandwidth, and high consistency among consecutive round trips leads to a high degree of coherence. The HBT measurement indicates high coherence and excellent consistency. We performed a fiber-based HOM interference measurement without any active stabilization. A conventional dip-type HOM interference with a raw visibility of 76.3% is obtained when testing single sideband. While frequency-entanglement is also demonstrated among the two sidebands via a spatial quantum beating with a fringe visibility of 97.9 %. Our results prove that the PI in active fiber cavity with fine structure and high tuning flexibility is attractive for the generation of highly coherent frequency-entangled quantum source, which would facilitate subsequent applications, including but not limited to quantum communications and quantum computing.

Methods

Details of the experimental setup. In our experiment, a ring fiber cavity contains 19.5 m dispersion compensation fiber (DCF), 10.1m single mode fiber (SMF), and 1 m erbium doped fiber (EDF). It's pumped by two 976 nm CW lasers with power of 400 mW, through two wavelength division multiplexers (WDMs). A polarization independent optical isolator (ISO) is used for unidirection operation. The cavity detuning is optimized by a polarization controller (PC). The output is traced from OC1 with a 10% output port. Additionally, a home-made saturable absorber (SA) is fabricated by filling reduced graphene oxide flakes into cladding holes of a photonic crystal fiber [22–25, 40]. The SA has a modulation depth of ~24%. The evanescent field interacting method permits only a very small percentage (10^{-7}) of light interacting with reduced graphene oxide. Therefore, the thermal damage threshold can be increased substantially, which is inaccessible for conventional film-based SA. In the ring cavity, the dispersion of EDF, DCF, and SMF are 15.7, -38, and 18 ps/nm/km, respectively, corresponding to a net normal dispersion of 0.863 ps². For this configuration, the fiber ring cavity together with the SA produce pulsed laser with nanosecond duration, whose peak power is high enough to excite PI sidebands under periodic dispersion management [23].

The optical spectrum is characterized by an optical spectrum analyzer with a resolution of 0.02 nm. Meanwhile, the corresponding single-shot spectra are recorded based on DFT detection, where periodic signals are stretched by a 500 m DCF

with a dispersion of 150 ps^2 for frequency-to-time mapping, and subsequently fed to a 50 GHz photodetector connecting to a real time oscilloscope with a bandwidth of 12.5 GHz. Therefore, the optical resolution of the DFT is about 25 GHz (0.2 nm in C band). After excitation of PI, the pulse intensity is attenuated by a variable optical attenuator (VOA), then the Stokes and anti-Stokes sidebands are filtered by two optical tunable filters (Santec, OTF-320) with a full width at half maximum bandwidth of 0.2 nm. The extinction of the filtered wavelengths with respect to the center wavelength is larger than 90 dB.

For the HOM interference measurement, a fiber-based MZI is constructed by two OCs, in which a fiber-coupled optical DL is inserted to tune the path difference. The correlation properties of the photon pairs are tested by HBT measurement as shown in Fig. 1(c). Here, after the VOA2, the photon pairs are separated by OC5, then the photons in two paths are filtered by two OTFs, respectively. The relative time delay of two paths is adjusted by a DL together with the electrical delay when accounting for coincidence counts. All fibers and optical devices are unpolarized. Importantly, the fiber-based MZI is running at room temperature without any stabilization techniques. Namely, there is not stable phase difference due to the influence of environment, and the induced path fluctuation would seriously deteriorate the two-photon interference visibility [41]. The photons in the two channels are detected by two identical InGaAs SPDs under Geiger-mode within a high speed near-infrared single photon detection module (Auréa Technology), then the coincidence counts are registered. The two SPDs are triggered by an internal trigger module at a rate of 1.25 MHz, and the quantum efficiency is 20%. The gate window is 5 ns, and the dead time is 10 μs .

Numerical simulations. When we considering a fiber ring cavity with varying dispersion, the optical field ψ evolution can be modeled by the nonlinear Schrödinger equation (NLSE) with varying Kerr nonlinearity γ and second order dispersion β_2 [22–25]

$$i \frac{\partial}{z} - \frac{\alpha^2}{2} \frac{\partial^2}{t^2} + |\psi|^2 + i \frac{\beta_2}{2} = 0 \quad (4)$$

where, α denotes the linear loss (positive) or amplification (negative), respectively. We ignore the higher order dispersion or Raman scattering, as they do not have a noticeable influence on the PI dynamics in our fiber cavity. Using the Floquet method transformation with the variable $U=\psi \exp(-\alpha z/2)$, one obtains from (5)

$$i \frac{\partial U}{z} - \frac{\alpha^2}{2} \frac{\partial^2 U}{t^2} + \beta'(z) |U|^2 U = 0 \quad (5)$$

where, $\beta'=\gamma \exp(-\alpha z)$. Supposing that $|U|^2 \ll P$, the perturbed CW solution of the NLSE (5) is as following,

$$U(z, t) = \left[\sqrt{P} + u(Z, T) \right] \exp\{iPz\} \quad (6)$$

Therefore, the linearized equation for $u(Z, T)$ is obtained as

$$iu_Z = -\frac{\alpha^2}{2} \frac{\partial^2 u}{\partial T^2} + \beta'(Z) (u + u^*) \quad (7)$$

where, $Z=z/L_{\text{nl}}$, and $T=t/t_0$ (the nonlinear length $L_{\text{nl}}=1/(\gamma P)$, the dispersion length $L_d=t_0^2/|\beta_{2\text{av}}|$, and the reference time unit $t_0=1$

ps). $\beta_2=L_{\text{nl}}/L_d$. $d(Z)=1+\beta_{2\text{amp}}/|\beta_{2\text{av}}| \sin(2\pi Z L_{\text{nl}}/\Lambda)$, where $\beta_{2\text{amp}}$ is the amplitude of the dispersion variation, $\beta_{2\text{av}}$ is the average dispersion of the cavity, Λ is the spatial period of the cavity.

By writing the solution of (7) as the sum of Stokes and anti-Stokes sidebands, $u(Z, T)=a(Z)\exp\{i\Omega T\}+b(Z)\exp\{-i\Omega T\}$, we obtain two coupled linear ordinary differential equations with periodic coefficients for $a(Z)$ and $b(Z)$

$$a_Z = i \frac{\partial}{Z} - \frac{\alpha^2}{2} d(Z) a + i \beta'(Z) (a + b) \quad (8.1)$$

$$b_Z = -i \frac{\partial}{Z} - \frac{\alpha^2}{2} d(Z) b - i \beta'(Z) (a + b) \quad (8.2)$$

A linear stability analysis of (8) can be rigorously carried out numerically by the Floquet theory.

According to the experimental conditions, we follow the above parameters for simulations. Additionally, Kerr nonlinearity γ is $2 \text{ W}^{-1}\text{km}^{-1}$, and a spatial period of the dispersion variation equal to the cavity length (30.6 m). The losses of the DCF, and the SMF are 0.5 dB/km, 0.2 dB/km, respectively. The gain of EDF compensates cavity loss exactly. An additional loss of 1dB is inserted for out-coupling loss and connector losses. The pulse duration is about 0.04 ns. The numerically computed PI sidebands for various peak powers are depicted in Fig. 2(a). Here, we focus on the fundamental sidebands, and neglect other high order sidebands as their energies are much lower.

Data availability. Data underlying the results presented in this paper are available upon reasonable request to the authors.

References

1. Gisin, N., Ribordy, G., Tittel, W. & Zbinden, H. Quantum cryptography. *Rev. Mod. Phys.* **74**, 145–195 (2002).
2. Ekert, A. K., Rarity, J. G., Tapster, P. R. & Massimo Palma, G. Practical quantum cryptography based on two-photon interferometry. *Phys. Rev. Lett.* **69**(9), 1293–1295 (1992).
3. Giovannetti, V., Lloyd, S. & Maccone, L. Quantum-enhanced measurements: beating the standard quantum limit. *Science* **306**, 1330–1336 (2004).
4. Jeong, H. Using weak nonlinearity under decoherence for macroscopic entanglement generation and quantum computation. *Phys. Rev. A* **72**, 34305 (2005).
5. Kues, M., Reimer, C., Roztocki, P., Cortés, L. R., Sciara, S. & Wetzel, B. et al. On-chip generation of high-dimensional entangled quantum states and their coherent control. *Nature* **546**, 622–626 (2017).
6. Giovannetti, V., Lloyd, S. & Maccone, L. Quantum-enhanced positioning and clock synchronization. *Nature* **412**, 417–419 (2001).
7. Nasr, M. B., Saleh, B. E. A., Sergienko, A. V. & Teich, M. C. Demonstration of dispersion-cancelled quantum-optical coherence tomography. *Phys. Rev. Lett.* **91**, 083601 (2003).
8. Hong, C. K. & Mandel, L. Theory of parametric frequency down conversion of light. *Phys. Rev. A* **31**, 2409 (1985).
9. Eisenberg, H. S., Khoury, G., Durkin, G. A., Simon, C. & Bouwmeester, D. et al. Editorial note: quantum entanglement of a large number of photons. *Phys. Rev. Lett.* **93**, 219901 (2004).
10. MacLean, J. W., Donohue, J. M. & Resch, K. J. Direct characterization of ultrafast energy-time entangled photon pairs. *Phys. Rev. Lett.* **120**, 053601 (2018).
11. Li, X., Voss, P. L., Sharpen, J. E. & Kumar, P. Optical-fiber source of polarization-entangled photons in the 1550 nm telecom band. *Phys. Rev. Lett.* **94**, 053601 (2005).
12. Zhou, Q., Zhang, W., Yuan, C., Huang, Y. & Peng, J. Generation of 1.5 μm discrete frequency-entangled two-photon state in polarization-maintaining fibers. *Opt. Lett.* **39**, 2109–2112 (2014).

13. Smith, B. J., Mahou, P., Cohen, O., Lundein, J. S. & Walmsley, I. A. Photon pair generation in birefringent optical fibers. *Opt. Express* **17**, 23589-23602 (2009).
14. Reimer, C., Kues, M., Roztocki, P., Wetzel, B., Grazioso, F., Little, B. E., Chu, S. T., Johnston, T., Bromberg, Y., Caspani, L., Moss, D. J. & Morandotti, R. Generation of multiphoton entangled quantum states by means of integrated frequency combs. *Science* **351**, 1176-1180 (2016).
15. Jaramillo-villegas, J. A., Imany, P., Odele, O. D., Leaird, D. E., Ou, Z. Y., Qi, M. & Weiner, A. M. Persistent energy-time entanglement covering multiple resonances of an on-chip biphoton frequency comb. *Optica* **4**, 655-658 (2017).
16. Sua, Y. M., Malowicki, J., Hirano, M. & Lee, K. F. Generation of high purity photon-pair in a short highly non-linear fiber. *Opt. Lett.* **38**, 73-75 (2013).
17. Palmett, K. G., Delgado, D. C., Serna, F. D., Ricardo, E. O., Ruz, J. M., Ramirez, H. C., Alarcon, R. R. & U'Ren, A. B. Photon-pair generation by intermodal spontaneous four-wave mixing in birefringent, weakly guiding optical fibers. *Phys. Rev. A* **93**, 033810 (2016).
18. Cui, L., Li, X. & Zhang, N. Spectral properties of photon pairs generated by spontaneous four-wave mixing in inhomogeneous photonic crystal fibers. *Phys. Rev. A* **85**, 023825 (2012).
19. Solli, D. R., Herink, G., Jalali, B. & Ropers, C. Fluctuations and correlations in modulation instability. *Nat. Photon.* **6**, 463-468 (2012).
20. Hong, C. K., Ou, Z. Y. & Mandel, L. Measurement of subpicosecond time intervals between two photons by interference. *Phys. Rev. Lett.* **59**, 2044-2046 (1987).
21. Liang, J., Hendrickson, S. M. & Pittman, T. B. Role of pump coherence in two-photon interferometry. *Phys. Rev. A* **83**, 033812 (2011).
22. Finot, C., Feng, F., Chembo, Y. & Wabnitz, S. Gain Sideband Splitting in Dispersion Oscillating Fibers. *Opt. Fiber Tech.* **20**, 513-519 (2014).
23. Gao, L., Zhu, T., Wabnitz, S., Liu, M. & Huang, W. Coherence loss of partially mode-locked fiber laser. *Sci. Rep.* **6**, 24995 (2016).
24. Conforti, M., Mussot, A., Kudlinski, A. & Trillo, S. Modulational instability in dispersion oscillating fiber ring cavities. *Opt. Lett.* **39**, 4200-4203 (2014).
25. Copie, F., Conforti, M., Kudlinski, A., Mussot, A. & Trillo S. Competing Turing and Faraday Instabilities in Longitudinally Modulated Passive Resonators. *Phys. Rev. Lett.* **116**, 143901 (2016).
26. Faraday, M. On a peculiar class of acoustical figures; and on certain forms assumed by groups of particles upon vibrating elastic surfaces. *London* **3**, 03655695 (1831).
27. Benjamin, T. B. & Ursell, F. The stability of the plane free surface of a liquid in vertical periodic motion. *Proc. R. Soc. A* **225**, 505 (1954).
28. Coullet, P., Frisch, T. & Sonnino, G. Dispersion-induced patterns. *Phys. Rev. E* **49**, 2087 (1994).
29. Engels P., Atherton C. & Hoefer M. A. Observation of Faraday waves in a Bose-Einstein condensate. *Phys. Rev. Lett.* **98**, 095301 (2007).
30. Perego, A. M., Tarasov, N., Churkin, D. V., Turitsyn, S. K. & Staliunas, K. Pattern generation by dissipative parametric instability. *Phys. Rev. Lett.* **116**, 028701 (2016).
31. Ou, Z. Y. & Lu, Y. J. Optical parametric oscillator far below threshold: Experiment versus theory. *Phys. Rev. Lett.* **62**, 033804 (1999).
32. Langerfeld, T. F., Meyer, H. M. & Köhl, M. Correlated-photon-pair emission from a cw-pumped Fabry-Perot microcavity. *Phys. Rev. A* **97**, 023822 (2018).
33. Shi, B. S. & Tomita, A. Generation of a pulsed polarization entangled photon pair using a Sagnac interferometer. *Phys. Rev. A* **69**, 013803 (2004).
34. Cosm, e O. & Padua, S. Hong-Ou-Mandel interferometer with one and two photon pairs. *Phys. Rev. A* **77**, 053822 (2008).
35. Giovannetti, V., Maccone, L., Shapiro, J. H. & Wong, F. N. C. Generating entangled two-photon states with coincident frequencies. *Phys. Rev. Lett.* **88**, 183602 (2002).
36. Kim, T. S., Kim, H. O., Ko, J. H. & Park, G. D. Two-photon interference experiment in a Mach-Zehnder interferometer. *J. Opt. Soc. Korea* **7**, 113 (2003).
37. Ou, Z. Y. & Mandel L. Observation of spatial quantum beating with separated photodetectors. *Phys. Rev. Lett.* **61**, 54 (1988).
38. Trenti, A., Borghi, M., Mancinelli, M., Price, H. M., Fontana, G. & Pavese, L. Quantum interference in an asymmetric Mach-Zehnder interferometer. *J. Opt.* **18**, 085201 (2016).
39. Takesue, H. 1.5- μ m band Hong-Ou-Mandel experiment using photon pairs generated in two independent optical fibers. *Appl. Phys. Lett.* **90**, 204101 (2007).
40. Gao, L., Zhu, T., Li, Y. J., Huang, W. & Liu, M. Watt-level ultrafast fiber laser based on weak evanescent interaction with reduced graphene oxide. *IEEE Photxon. Technol. Lett.* **28**, 1245 (2016).
41. Cho, S. B. & Kim, H. Active stabilization of a fiber-optic two-photon interferometer using continuous optical length control. *Opt. Express* **24**, 10980 (2016).
42. Hu, Y., Peng, X., Li, T., & Guo, H. On the Poisson Approximation to Photon Distribution for Faint Lasers. *Phys. Lett. A* **367**, 173 (2007).
43. Wang, T., Aktas, D., Alibart, O., Picholle, E., Puccioni, G. P., Tanzilli, S. & Lippi, G. L. Superthermal-light emission and nontrivial photon statistics in small lasers. *Phys. Rev. A* **101**, 063835 (2020).

Acknowledgments.

Natural Science Foundation of China (61635004, 62075021); National Science Fund for Distinguished Young Scholars (61825501). European Union's Horizon 2020 research and innovation program under a Marie Skłodowska-Curie program (691051); Russian Ministry of Science and Education (14.Y26.31.0017). We appreciate the discussion with Prof. Qiang Zhou from University of Electronic Science and Technology of China.

Author contributions.

L. G., Z. L., H. R., Y. C., Z. X., S. D., Q. W., and L. K. built up the experimental setup, performed the experimental investigation, and data analysis. S. W. performed the theoretical investigations. L. H., and W. H. provided resources. T. Z. supervised the project. All authors interpreted and discussed the results.

Competing interests.

The authors declare no conflicts of interest.